# Eulerian-Eulerian simulation of dusty gas flows past a prism from subsonic to supersonic regimes using a modal discontinuous Galerkin method

Omid Ejtehadi [a,b], R. S. Myong[a*]

[a] *School of Mechanical and Aerospace Engineering, and ACTRC & ReCAPT, Gyeongsang National University, Jinju, Gyeongnam 52828, South Korea*

[b] *Supercomputing Modeling and Simulation Center, Korea Institute of Science and Technology Information (KISTI), Daejeon 305-806, South Korea*

*Corresponding author: Tel +82 55 772-1645 (Fax 1580); *myong@gnu.ac.kr*

**Abstract**

The present work investigates the bubble formation and vortex shedding phenomena in the viscous flow of a compressible gas seeded with dust particles. A new modal discontinuous Galerkin method was developed for solving the two-fluid model of dusty gas flows. Most previous studies have been limited to flows with low Mach numbers without the presence of shock waves. This study considered a wider Mach number range, from subsonic to supersonic, in the presence of shock waves. We also investigated in detail the effects of the presence of solid particles on flow properties such as bubble size and frequency and the amplitude of the Bérnard-von Kármán vortex street. A novel approach was employed to circumvent the non-strictly hyperbolic nature of the equations of the dusty-gas flow model caused by the non-existence of the pressure term. This allowed the same inviscid numerical flux functions to be applicable for both the gaseous Euler and solid pressureless-Euler systems. The simulation results revealed that the transition from stationary flow to unsteady flow is dependent on both the Reynolds and Mach numbers of the flow. Moreover, it was shown that in stark contrast with the pure gas case above the critical Reynolds number in the supersonic regime, where no flow instability was observed, in the multiphase flows, adding particles produced flow instability. This unusual behavior is because the two-way coupling effects between the gas phase and solid phase override the compressibility effect and cause severe flow instability and spontaneous symmetry breaking in the coherent dynamics of the vortices.

**Keywords**: discontinuous Galerkin, dusty gas, Eulerian-Eulerian, vortex shedding, coupling effects

## 1. Introduction

Flow past bluff bodies is an important subject because they appear in a diverse number of applications, including the aerodynamic designs of flying objects and structures on the ground, electronic cooling, aeroacoustic noise, convective heat exchangers, and flow dividers. The shape and size of the bluff body influence the location of flow separation as well as wake dynamics behind the body. The location of separation on bodies with smooth surfaces (circular or elliptical cylinders) depends on the geometry of the body and the state of the boundary layer, as defined by the free-stream Reynolds number. In contrast, on bodies with sharp-edged surfaces (triangular or rectangular prisms), the location depends only on the shape of the body.

It is also well known that above a certain Reynolds number (*critical Reynolds number* $Re_{cr}$), stable flow around the bluff body becomes unstable, initiating the onset of the so-called *von Kármán vortex street*. The Bérnard-von Kármán instability leads to the deformation of symmetrical twin vortices (bubbles), and the vortices are shed with frequencies defined by Strouhal number. The vortex shedding phenomenon can occur in laminar or turbulent flows. Plenty of research articles have investigated these crucial features, both experimentally and numerically.

The problem of flows past bluff bodies like circular and square cylinders has been well-reviewed and documented by many researchers [1-11]. However, very few studies have focused on flows past triangular prisms. Jackson [12] reported the critical Reynolds number to be 34.3 for isosceles triangles with base 1.0 and height 0.8. In another numerical investigation, Zielinska and Wesfreid [13] reported a critical Reynolds number of 38.3 for flow past an equilateral triangular prism with a blockage ratio of 1.15. This finding was further confirmed in experiments by Goujon-Durand et al. [14] and Wesfreid *et al*. [15]. Johansson *et al*. [16] investigated the turbulent flow past a triangular cylinder using the $k$-$\varepsilon$ turbulence model. De and Dalal [17] investigated two-dimensional laminar flow past a triangular cylinder and predicted a critical Reynolds number of 39.9.

Other crucial features like the time-averaged drag coefficient, the root mean square values of lift, and the Strouhal number have also been studied in the past. Prhashanna *et al*. [18] conducted comprehensive numerical investigations on the influence of the index of power-law fluids on the formation of the wake, and the onset of vortex shedding in flow across an equilateral triangular cylinder. The effects of Reynolds number and Prandtl number on the

drag coefficients and heat transfer in the steady regime were also investigated. Further, Chatterjee and Mondal [19] investigated the characteristics of forced convection heat transfer for flow past a long heated equilateral triangular cylinder in an unconfined medium in the low Reynolds number laminar regime. However, very few works have explored the effects of Reynolds number in a flow regime with high Mach numbers beyond the incompressible limit.

The influence of dust particles on viscous flows is another important subject requiring further investigation. This problem can be found in many natural phenomena like soil erosion by natural winds or volcanic eruptions, and engineering applications like the purification of crude oil in the petroleum industry, the enhancement of heat transfer processes with the use of dust, in dust/mist/fume collators in gas cooling systems or even in the decent phase of a Lunar landing [20]. The importance of better understanding such two-way coupling effects has motivated extensive numerical experiments, investigating the influence of particles on the steady and unsteady behavior of vortices [21].

Considerable efforts have been devoted to investigating the interaction of particles with vortices in the past, for applications like combustion systems, wire and plate electrostatic precipitators, and the spread of fires by firebrands [21, 22]. Saffman [23] showed that for fine dust particles, the addition of dust can destabilize a gas flow, while for coarse-grain particles, the addition of dust can stabilize gas flows. Damseh [24] investigated a viscous incompressible flow of gas across an isothermal cylinder in the presence of a cloud of uniform dust particles. Mehrizi *et al*. [25] investigated the effect of nanoparticles on natural convection heat transfer in a two-dimensional horizontal internal flow in an annulus made up of a heated triangular inner cylinder and a circular outer cylinder.

In a more recent study, Xu *et al*. [26] investigated the behavior of fine particles in the laminar flow of air past a triangular prism both experimentally and numerically. Bai and Li [27] investigated the motion and deposition of particles in a supersonic flow past a wedge using an Eulerian-Lagrangian numerical model. *The present study may be considered the first to attempt a simulation of dusty gas flow past bluff bodies from subsonic to supersonic regimes in an Eulerian-Eulerian framework.*

In recent decades, the discontinuous Galerkin (DG) method [28-37] has become a popular method for solving a system of conservation laws. In this study, we first develop a new modal discontinuous Galerkin method, for solving the two-fluid model of dusty gas flows. We then investigate the effects of coupling in the gaseous and solid phase on symmetrical vortices, the

onset of unsteadiness, and the frequency of the vortex shedding. We limit our investigation here to the laminar flow case. A set of numerical experiments was selected based on the Reynolds and Mach numbers from subsonic to supersonic regimes.

The Mach number regime based on the conventional categorization can be divided into low subsonic (incompressible limit, $M < 0.3$ ), subsonic ( $0.3 < M < 0.8$ ), transonic ($0.8 < M < 1.2$), and supersonic ($1.2 < M < 5.0$) regimes. In setting up the test cases, the Mach numbers were selected in a way to cover almost the entire range. Moreover, we focused on the low Reynolds laminar flows before and after the onset of the vortex shedding phenomena characterized by the critical Reynolds number. The range of flow conditions simulated in this work is summarized in **Table 1**.

**Table 1** Categories of regimes based on the Reynolds and Mach numbers and regimes considered in this work

Pure gas

| | $Re<Re_{cr}$ | $Re>Re_{cr}$ |
|---|---|---|
| M=0.1 | ✓ | ✓ |
| M=0.3 | ✓ | ✓ |
| M=0.8 | ✓ | ✓ |
| M=1.2 | ✓ | ✓ |
| M=2.0 | ✓ | ✓ |

Dusty gas

| | $Re<Re_{cr}$ | $Re>Re_{cr}$ | Loading ratio ($\beta$) |
|---|---|---|---|
| M=0.1 | ✓ | ✓ | ✓ |
| M=1.2 | ✓ | ✓ | ✓ |

## 2. Theoretical formulation

Among the three primary models for modeling particulate flows, i.e., the Eulerian-Eulerian, Eulerian-Lagrangian, and mixture models, the Eulerian-Eulerian model was selected because of its efficiency in terms of computational cost. In the majority of two-fluid models for dusty gas flows, the gas phase is considered to be compressible, which follows the perfect-gas law, while the solid phase is considered incompressible [38-41]. The inter-particle collisions are neglected (thus there is no pressure term in the conservation laws of the solid phase), and the particles are assumed to be uniform sized spheres with a constant diameter, density, and temperature. The specific heat of the particle material is also assumed to be constant. Moreover, particles are considered to be inert and the thermal and Brownian motions of particles are neglected. The gravitational and buoyant forces, the turbulence effects, and the effect of the particles' wakes are considered to be negligible. In this model,

the number density of the particles should be large enough not to violate the continuum assumption.

2.1. Mathematical model of viscous dusty gases

Under the aforementioned conditions, the conservation law can be written as follows: for the gas phase,

$$\partial_t \mathbf{U}_g + \nabla \cdot \mathbf{F}_g = \mathbf{S} \tag{1}$$

$$\mathbf{U}_g = \begin{bmatrix} \alpha_g \rho_g \\ \alpha_g \rho_g \mathbf{u}_g \\ \alpha_g \rho_g E_g \end{bmatrix}, \quad \mathbf{F}_g = \begin{bmatrix} \alpha_g \rho_g \mathbf{u}_g \\ \alpha_g \rho_g \mathbf{u}_g \mathbf{u}_g + p\mathbf{I} + \mathbf{\Pi}_g \\ (\alpha_g \rho_g E_g + p)\mathbf{u}_g + \mathbf{\Pi}_g . \mathbf{u}_g + \mathbf{Q}_g \end{bmatrix},$$
$$\mathbf{S} = \begin{bmatrix} 0 \\ D_{g,s}(\mathbf{u}_s - \mathbf{u}_g) \\ D_{g,s}(\mathbf{u}_s - \mathbf{u}_g)\mathbf{u}_s + Q_g(T_s - T_g) \end{bmatrix}, \tag{2}$$

$$E_g = c_v T_g + \frac{1}{2}\left|\mathbf{u}_g\right|^2, \tag{3}$$

and for the solid phase,

$$\partial_t \mathbf{U}_s + \nabla \cdot \mathbf{F}_s = -\mathbf{S}, \tag{4}$$

$$\mathbf{U}_s = \begin{bmatrix} \alpha_s \rho_s \\ \alpha_s \rho_s \mathbf{u}_s \\ \alpha_s \rho_s E_s \end{bmatrix}, \quad \mathbf{F}_s = \begin{bmatrix} \alpha_s \rho_s \mathbf{u}_s \\ \alpha_s \rho_s \mathbf{u}_s \mathbf{u}_s \\ (\alpha_s \rho_s E_s)\mathbf{u}_s \end{bmatrix}, \tag{5}$$

$$E_s = c_m T_p + \frac{1}{2}\left|\mathbf{u}_s\right|^2, \tag{6}$$

$$\alpha_g + \alpha_s = 1. \tag{7}$$

Here the **U**, **F,** and **S** are conservative variables, fluxes, and source terms, respectively. The variables *t, α, ρ,* **u**, *E*, *p*, *T*, *D*, and *Q* represent time, volume fraction, density, velocity vector, total energy, pressure, temperature, interphase drag, and heat transfer, respectively. The density of dust particles $\rho_s$ is assumed to be constant. $c_v$ and $c_m$ are the specific heat capacity of the gas at constant volume and the specific heat of the particle material. The equation of state expresses the gas pressure in terms of other gas properties:

$$p = \rho_g R T_g, \tag{8}$$

where *R* is the gas constant.

According to Miura and Glass [42], the drag force acting on a solid particle by the gas phase can be expressed as

$$D_{g,s} = \frac{3}{4} C_D \frac{\alpha_s \rho_g}{d} \left| \mathbf{u}_g - \mathbf{u}_s \right|, \tag{9}$$

where $d$ is the particle diameter and $C_D$ is the drag coefficient computed as a function of the Reynolds number based on the particle diameter and relative velocity of the particle to the gas (i.e. $\mathrm{Re}_d = \rho_g d \left| \mathbf{u}_g - \mathbf{u}_s \right| / \mu_g$ ). The drag coefficient can then be given by a well-established semi-empirical correlation [43],

$$C_D = \begin{cases} \dfrac{24}{\mathrm{Re}_d} \left( 1 + 0.15 \mathrm{Re}_d^{\,0.687} \right) & \text{if} \quad \mathrm{Re}_d < 1000, \\ 0.44 & \text{if} \quad \mathrm{Re}_d > 1000. \end{cases} \tag{10}$$

The heat transfer, which is proportional to temperature difference, can be expressed as a function of the Nusselt number,

$$Q_g = \frac{6 \mathrm{Nu} \kappa_g}{d^2} \alpha_s (T_g - T_s), \tag{11}$$

$$\mathrm{Nu} = 2 + 0.65 \mathrm{Re}_d^{\frac{1}{2}} \mathrm{Pr}^{\frac{1}{3}}, \ \mathrm{Pr} = \frac{c_p \mu_g}{\kappa_g}. \tag{12}$$

Here $\mu_g$ and $\kappa_g$ represent the viscosity and thermal conductivity of the gas, respectively.

2.2. Dimensionless form of the equations

The following dimensionless variables and parameters are used to derive the non-dimensional governing system of equations. Here the dimensionless parameters are superscripted by *, and the subscript *ref* denotes the reference values,

$$\begin{gathered} \mathbf{x}^* = \frac{\mathbf{x}}{L}, \quad t^* = \frac{t}{t_{ref}}, \quad \mathbf{u}^* = \frac{\mathbf{u}}{u_{ref}}, \quad T^* = \frac{T}{T_{ref}}, \quad \rho^* = \frac{\rho}{\rho_{ref}}, \quad p^* = \frac{p}{p_{ref}}, \\ E^* = \frac{E}{E_{ref}}, \quad Q^* = \frac{Q}{Q_{ref}}, \quad \mu^* = \frac{\mu}{\mu_{ref}}, \quad \kappa^* = \frac{\kappa}{\kappa_{ref}}, \\ c_p{}^* = \frac{c_p}{c_{p_{ref}}}, \quad c_v{}^* = \frac{c_v}{c_{v_{ref}}}. \end{gathered} \tag{13}$$

In the above relations, $\mathbf{x}$ and $c_p$ are the spatial coordinates and the specific heat capacity at constant pressure, respectively. We then define the references and non-dimensional parameters as follows:

$$t_{ref} = \frac{L}{u_{ref}}, \quad \tau_s = \frac{\rho_s d_s^2}{18\mu_{ref}} \quad E_{ref} = u_{ref}^2, \quad Q_{ref} = \frac{\kappa_{ref}\Delta T_{ref}}{L},$$

$$\mathrm{M} = \frac{u_{ref}}{a_{ref}}, \quad \mathrm{Re} = \frac{\rho_{ref} u_{ref} L}{\mu_{ref}}, \quad \mathrm{Pr} = \frac{\mu_{ref} C_{p_{ref}}}{\kappa_{ref}}, \quad \mathrm{Pe} = \mathrm{Re}\,\mathrm{Pr},$$

$$\gamma = \frac{C_{p_{ref}}}{C_{v_{ref}}}, \quad \frac{1}{N_\delta \,\mathrm{Re}} = \frac{p_{ref}}{\rho_{ref} u_{ref}^2}, \tag{14}$$

$$N_\delta = \frac{\mu_{ref} u_{ref}}{p_{ref} L}, \quad \frac{1}{\mathrm{Re}\,\mathrm{Pr}\,\mathrm{Ec}} = \frac{1}{\mathrm{Pe}} \frac{C_{p_{ref}} T_{ref}}{u_{ref}^2},$$

$$St = \frac{\rho_{ref} u_{ref}}{D_{g,s} L}, \quad Nu = \frac{Q_s L^2}{k_{ref}}, \quad Ec = \frac{u_{ref}^2}{C_{p_{ref}} T_{ref}}.$$

After applying these definitions to equations (1) and (4), the following non-dimensional system of equations can be derived:

$$\partial_t \mathbf{U}_g + \nabla \cdot \mathbf{F}_g = \mathbf{S},$$

$$\mathbf{U}_g = \begin{bmatrix} \alpha_g \rho_g \\ \alpha_g \rho_g \mathbf{u}_g \\ \alpha_g \rho_g E_g \end{bmatrix},$$

$$\mathbf{F}_g = \begin{bmatrix} \alpha_g \rho_g \mathbf{u}_g \\ \alpha_g \rho_g \mathbf{u}_g \mathbf{u}_g + \dfrac{1}{N_\delta \,\mathrm{Re}}\, p\mathbf{I} + \dfrac{1}{\mathrm{Re}} \mathbf{\Pi}_g \\ (\alpha_g \rho_g E_g + \dfrac{1}{N_\delta \,\mathrm{Re}}\, p)\mathbf{u}_g + \dfrac{1}{\mathrm{Re}} \mathbf{\Pi}_g . \mathbf{u}_g + \dfrac{1}{Ec\,\mathrm{Pr}\,\mathrm{Re}} \mathbf{Q}_g \end{bmatrix}, \tag{15}$$

$$\mathbf{S} = \begin{bmatrix} 0 \\ \dfrac{1}{St}(\mathbf{u}_s - \mathbf{u}_g) \\ \dfrac{1}{St}(\mathbf{u}_s - \mathbf{u}_g).\mathbf{u}_s + \dfrac{\mathrm{Nu}}{EcPe}(T_s - T_g) \end{bmatrix}.$$

$$\partial_t \mathbf{U}_s + \nabla \cdot \mathbf{F}_s = -\mathbf{S},$$

$$\mathbf{U}_s = \begin{bmatrix} \alpha_s \rho_s \\ \alpha_s \rho_s \mathbf{u}_s \\ \alpha_s \rho_s E_s \end{bmatrix}, \quad \mathbf{F}_s = \begin{bmatrix} \alpha_s \rho_s \mathbf{u}_s \\ \alpha_s \rho_s \mathbf{u}_s \mathbf{u}_s \\ (\alpha_s \rho_s E_s)\mathbf{u}_s \end{bmatrix}. \tag{16}$$

Here the superscript * has been omitted for the sake of simplicity. The reference values for the length, pressure, temperature, and velocity are defined for each test case depending upon the problem under investigation.

## 3. Numerical method

The equations of the dusty gas flow described in the previous section can be discretized using a modal discontinuous Galerkin (DG) method. The essential parts of the modal unstructured DG method developed in the present work—in particular, the high order accuracy and positivity/monotonicity preserving property—were summarized in [44]. The discontinuous Galerkin method seems to be a natural choice for simulating dusty gas flows from subsonic to supersonic regimes for several reasons.

Apart from the distinguishing features provided by DG schemes, including compact stencil, parallelizability, and the ability to handle adaptive strategies, the method offers a special feature for simulating the dispersed particles in a gas. To resolve the important features of many types of flows, such as a supersonic compressible flow, fine computational grids are in general necessary.

An important constraint imposed on the computational grid for accurately simulating solid-gas multiphase flows, whether in the Eulerian or Lagrangian framework, is the minimum cell volume, which should be coarse enough to accommodate enough particles of certain diameters so that the solid phase can be considered a fluid. High order methods such as DG can achieve a higher order of accuracy even in coarser grids, through the use of high order polynomial expansions. In the following subsections, the essential features of the present DG scheme will be outlined briefly.

### 3.1. A modal discontinuous Galerkin method for simulating viscous dusty gas flows

The mathematical model of inviscid two-phase flows can be written in a compact form,

$$\partial_t \mathbf{U} + \nabla \cdot \mathbf{F}(\mathbf{U}) = \mathbf{S}(\mathbf{U}) \qquad \text{in} \left[ (t, \Omega) \middle| t \in (0, \infty), \Omega \subset \mathbb{R} \right], \tag{17}$$

where $\Omega$ denotes a bounded domain, and $\mathbf{U}$, $\mathbf{F}$, $\mathbf{S}$ are conservative variables vector, flux tensor, and source terms vector, respectively. The solution domain can be decomposed by a group of non-overlapping elements, $\Omega = \Omega_1 \cup \Omega_2 \cup ... \Omega_n$, in which $n$ is the number of elements. By multiplying a weighting function $\varphi_i$ into the conservative laws (13) and integrating over the control volume for each element, the following formulation can be derived:

$$\int_{\Omega_k} \left[ \partial_t \mathbf{U} \varphi(\mathbf{x}) + \nabla \cdot \mathbf{F}(\mathbf{U}) \varphi(\mathbf{x}) - \mathbf{S}(\mathbf{U}) \varphi(\mathbf{x}) \right] d\Omega = 0 . \tag{18}$$

In order to construct a discretized system of the conservation laws, the global spatial domain $\Omega$ can be approximated by $\Omega_h$ where $\Omega_h \rightarrow \Omega$ as $h \rightarrow 0$. The approximated domain, which is a tessellation of the space by bounded elementary control volumes, $\mathcal{T}_h = \{\Omega_e\}$, is filled with $n$

number of the non-overlapping elements $\Omega_e \in \mathcal{T}_h$ . The exact solution of the governing equations can be approximated by the numerical solution in every local element as

$$\mathbf{U}(\mathbf{x},t) \approx \mathbf{U}_h = \sum_{e=1}^{n} \mathbf{U}_h^e(\mathbf{x},t) \equiv \mathbf{U}_h^1 + \ldots + \mathbf{U}_h^n . \tag{19}$$

By splitting the integral over $\Omega_h$ into a series of integrals over the sub-elements and applying the integration by part, as well as the divergence theorem, to the equation (18), the elemental formulation reads as

$$\begin{aligned} \int_{\Omega_k} \partial_t \mathbf{U}_h \varphi_i(\mathbf{x}) \mathrm{d}\Omega_k + \oint_{\partial\Omega_k} \varphi_i(\mathbf{x}) \mathbf{F}(\mathbf{U}_h) \cdot \hat{n} d\sigma - \int_{\Omega_k} \nabla \varphi_i(\mathbf{x}) \cdot \mathbf{F}(\mathbf{U}_h) \mathrm{d}\Omega_k \\ = \int_{\Omega_k} \varphi_i(\mathbf{x}) \mathbf{S}(\mathbf{U}_h) \mathrm{d}\Omega_k , \end{aligned} \tag{20}$$

where $\hat{n}$ is the outward normal vector of the element interface, and $\mathbf{U}_h$ is the *p*-exact polynomial approximated solutions of the $\mathbf{U}$ on the discretized domain of $\Omega_h$. $\mathbf{U}_h$ can be expressed as the polynomial field that sums the multiplication of the local degree of freedom with the corresponding smooth polynomials of degree *P* in the standard element:

$$\mathbf{U}_h = \sum_{i}^{P} a_i(t) \varphi_i(\mathbf{x}) . \tag{21}$$

Here $a_i(t)$ and $\varphi(\mathrm{x})$ denote the local degree of freedom and the basis function, which can be chosen to be any continuous polynomial function, respectively.

The mathematical model of interest in the present work (with the inclusion of viscous terms for the gas phase) can be written in the following compact form:

$$\partial_t \mathbf{U} + \nabla \cdot \mathbf{F}_{\text{inv}}(\mathbf{U}) + \nabla \cdot \mathbf{F}_{\text{vis}}(\mathbf{U}, \nabla \mathbf{U}) = \mathbf{S}(\mathbf{U}) \qquad \text{in} \left[ (t, \Omega) \middle| t \in (0, \infty), \Omega \subset \mathbb{R} \right]. \tag{22}$$

As can be seen in (22), when the solution of viscous flows is of interest, an approach for estimating the derivatives of the conserved variable that appear in the viscous flux terms should be applied. In this regard, second-order derivatives required in the estimation of the viscous fluxes cannot be accommodated directly in a weak variational formulation using a discontinuous space function. One possible approach is the addition of a set of separate equations to treat the gradient of the conservative variables as an auxiliary set of unknowns, as proposed by Bassi and Rebay [28]. In this work, a matrix $\mathbf{A}$ is chosen to be the derivatives of the conserved variables $\mathbf{U}$, i.e., $\mathbf{A} = \nabla \mathbf{U}$ . This approach is known as the mixed DG formulation and will result in the following coupled system:

$$\begin{aligned} \mathbf{A} - \nabla \mathbf{U} &= 0, \\ \partial_t \mathbf{U} + \nabla \cdot \mathbf{F}_{\text{inv}}(\mathbf{U}) + \nabla \cdot \mathbf{F}_{\text{vis}}(\mathbf{U}, \nabla \mathbf{U}) &= \mathbf{S}(\mathbf{U}). \end{aligned} \tag{23}$$

In a similar way to (19),

$$\mathbf{U}_h = \sum_i^P U_i(t)\varphi_i(\mathbf{x}) \text{ and } \mathbf{A}_h = \sum_i^P A_i(t)\varphi_i(\mathbf{x}), \tag{24}$$

where $A_i(t)$ denotes the local degree of freedom for the auxiliary variable, we have

$$\int_{\Omega_k} \left[\mathbf{A}\varphi(\mathbf{x}) - \nabla \mathbf{U}\varphi(\mathbf{x})\right] d\Omega = 0, \tag{25}$$

$$\int_{\Omega_k} \left[\partial_t \mathbf{U}\varphi(\mathbf{x}) + \nabla \cdot \mathbf{F}_{\text{inv}}(\mathbf{U})\varphi(\mathbf{x}) + \nabla \cdot \mathbf{F}_{\text{vis}}(\mathbf{U})\varphi(\mathbf{x}) - \mathbf{S}(\mathbf{U})\varphi(\mathbf{x})\right] d\Omega = 0, \tag{26}$$

$$\int_{\Omega_k} \varphi_i(\mathbf{x})\mathbf{A}_h \mathrm{d}\Omega_k - \oint_{\partial\Omega_k} \varphi_i(\mathbf{x})\mathbf{U}_h \cdot \hat{n} d\sigma + \int_{\Omega_k} \nabla \varphi_i(\mathbf{x}) \cdot \mathbf{U}_h \mathrm{d}\Omega_k = 0, \tag{27}$$

$$\begin{aligned} &\int_{\Omega_k} \partial_t \mathbf{U}_h \varphi_i(\mathbf{x}) \mathrm{d}\Omega_k + \oint_{\partial\Omega_k} \varphi_i(\mathbf{x})\mathbf{F}_{\text{inv}}(\mathbf{U}_h) \cdot \hat{n} d\sigma - \int_{\Omega_k} \nabla \varphi_i(\mathbf{x}) \cdot \mathbf{F}_{\text{inv}}(\mathbf{U}_h) \mathrm{d}\Omega_k \\ &+ \oint_{\partial\Omega_k} \varphi_i(\mathbf{x})\mathbf{F}_{\text{vis}}(\mathbf{U}_h) \cdot \hat{n} d\sigma - \int_{\Omega_k} \nabla \varphi_i(\mathbf{x}) \cdot \mathbf{F}_{\text{vis}}(\mathbf{U}_h) \mathrm{d}\Omega_k = \int_{\Omega_k} \varphi_i(\mathbf{x})\mathbf{S}(\mathbf{U}_h) \mathrm{d}\Omega_k. \end{aligned} \tag{28}$$

The process of estimating the surface and volume integrals is analogous to the inviscid system procedure. However, for the auxiliary terms, a central flux splitting scheme is applied,

$$\begin{aligned} \mathbf{F}_{\text{vis}}(\mathbf{U}_h) \approx \hat{\mathrm{f}}_{i,\text{vis}}\left(\mathbf{U}_h^-, \mathbf{A}_h^-, \mathbf{U}_h^+, \mathbf{A}_h^+\right) &= \frac{1}{2}\left[\mathbf{F}_{i,\text{vis}}\left(\mathbf{U}_h^-, \mathbf{A}_h^-\right) + \mathbf{F}_{i,\text{vis}}\left(\mathbf{U}_h^+, \mathbf{A}_h^+\right)\right], \\ \mathbf{U} \approx \hat{\mathrm{f}}_{i,\text{aux}}\left(\mathbf{U}_h^-, \mathbf{U}_h^+\right) &= \frac{1}{2}\left[\mathbf{U}_h^- + \mathbf{U}_h^+\right]. \end{aligned} \tag{29}$$

3.2. Positivity and monotonicity preserving (limiting) procedure

High order conservative schemes, including the DG scheme introduced in the previous section, usually suffer from non-physical negative density or pressure. This situation leads to the ill-posedness of the system and numerical breakdowns as a consequence. On the other hand, for conservation laws with source terms which are added to account for chemical reactions, gravity, or the interaction of phases, as in the present case, there is a higher possibility of encountering negative density or pressure during the numerical simulation. Therefore, the application of efficient positivity preserving schemes is necessary to prevent numerical breakdown.

In the present work, the positivity preserving scheme of Zhang and Shu [45], developed for compressible Euler equations, were employed to ensure the positivity of density and pressure fields, while maintaining higher-order accuracy. Our numerical studies show that the mere application of the positivity preserving scheme is not enough to develop a stable scheme,

especially in the presence of strong shock waves. The situation deteriorates when a multiphase system with source terms is solved.

In order to ensure the preservation of scheme monotonicity, we employ the limiter of Zhang and Shu [46] developed for one-dimensional cases, and the limiter of Barth and Jespersen [47] initially devised for a finite volume framework. It is important to note that any TVD/MUSCL type scheme can degrade the order of accuracy in the smooth regions of the solution unless a pragmatic shock detection scheme is introduced.

3.3. Circumventing the non-strict hyperbolicity of the dusty gas model equation

The non-strictly hyperbolic nature of the dust phase equation (due to the non-existence of a pressure term) can impose serious difficulties on the numerical solver (especially when finite volume schemes are applied). In this study, a simple but effective strategy is introduced to remedy this issue, which has long been considered a challenging task. The basic idea was inspired by a strategy initially developed in computational magnetohydrodynamics (MHD) [48-50] which has since been applied in other fields, including aircraft and wind turbine icing in the atmosphere [51]. Here we apply the approach to treat the two-fluid equation model of dusty gases.

The idea is to add and subtract a pressure-related term to the momentum and energy equations of the dust phase. Even though this action does not have any mathematical consequences, from a numerical point of view, the new system recovers the strict hyperbolicity of the equation. The equations of the dust phase after the addition and subtraction of a pressure-related term can be written as follows,

$$\partial_t \begin{bmatrix} \alpha_s\rho_s \\ \alpha_s\rho_s\mathbf{u}_s \\ \alpha_s\rho_s E_s \end{bmatrix} + \nabla\cdot \begin{bmatrix} \alpha_s\rho_s\mathbf{u}_s \\ \alpha_s\rho_s\mathbf{u}_s\mathbf{u}_s + p_s\mathbf{I} - p_s\mathbf{I} \\ (\alpha_s\rho_s E_s + p_s - p_s)\mathbf{u}_s \end{bmatrix} = -\mathbf{S}\,. \tag{30}$$

Equivalently in split form,

$$\partial_t \begin{bmatrix} \alpha_s\rho_s \\ \alpha_s\rho_s\mathbf{u}_s \\ \alpha_s\rho_s E_s \end{bmatrix} + \nabla\cdot \begin{bmatrix} \alpha_s\rho_s\mathbf{u}_s \\ \alpha_s\rho_s\mathbf{u}_s\mathbf{u}_s + p_s\mathbf{I} \\ (\alpha_s\rho_s E_s + p_s)\mathbf{u}_s \end{bmatrix} = -\mathbf{S} + \nabla\cdot \begin{bmatrix} 0 \\ p_s\mathbf{I} \\ p_s\mathbf{u}_s \end{bmatrix}. \tag{31}$$

In this equation, the inviscid flux is equivalent to that of the Euler equation of the gas phase. Thus, the conservation law on the left-hand side can be considered strictly hyperbolic, while the additional term in the right-hand side can be handled in exactly the same way the source terms are treated.

The equation of state for the dust pressure has been derived previously based on the kinetic theory of gases and is readily available in the present flow problem. Readers are referred to the comprehensive review by van der Hoef *et al*. [52] and references therein for further details on the derivation and formulation of the pressure term of the solid phase.

## 4. Numerical results

Schematics of the computational domain, boundary conditions, and grid are outlined in **Fig. 1**. Far-field and outflow boundary conditions are defined at a distance far enough from the prism. Grids with a total of 14,214 elements were used, and finer grids were located in the regions where flows were expected to evolve more severely.

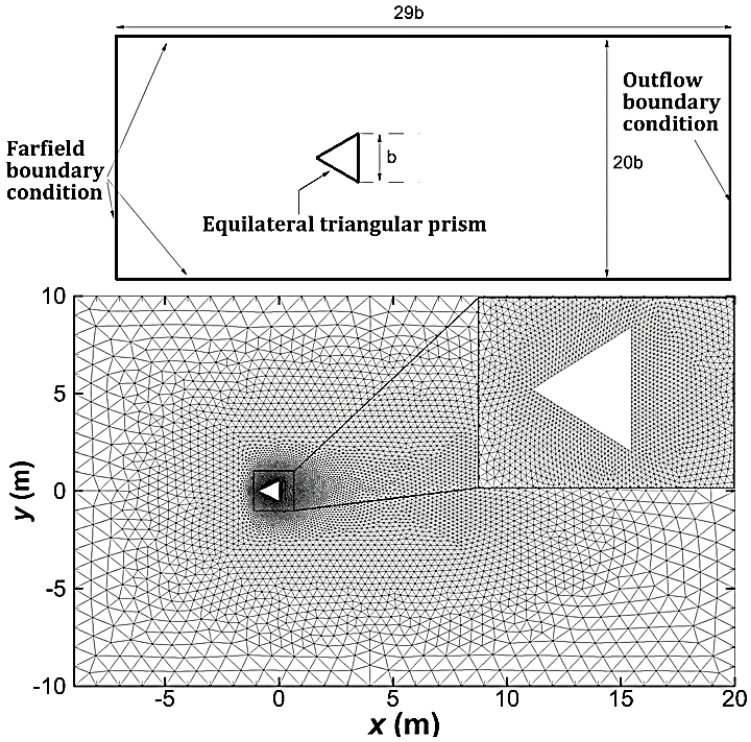


**Fig. 1** Computational domain, boundary conditions, and grid.

### 4.1. Validation of the numerical solutions

The numerical solutions for the gas phase were validated by comparing them with the results of De and Dalal [17, 53] and Zeitoun *et al*. [17, 53] in drag coefficients, as shown in **Fig. 2**. A spatially second-order accurate scheme with first-order polynomials ($P^1$) was used in conjunction with a third-order time-accurate Runge-Kutta scheme. Our numerical experiments showed that for the grids depicted in **Fig. 1**, a spatially first-order accurate scheme with zero-order polynomials ($P^0$) cannot capture the transition from steady to unsteady flow patterns. However, good agreement with previous results was observed

when a second-order accurate ($P^1$) scheme was used, especially for medium and high Reynolds number cases.

On the other hand, a small discrepancy was observed when compared with the result from Zeitoun *et al*. [53] for low Reynolds number cases. The gap may be due to differences in the mathematical and computational formulations (pressure-based vs. density-based), numerical approaches (finite volume vs. discontinuous Galerkin), and computational grids (quadrilateral vs. triangular). However, the magnitude of this deviation was negligible (<10%). More validation studies on two-phase test cases can be found in works [44, 54-56].

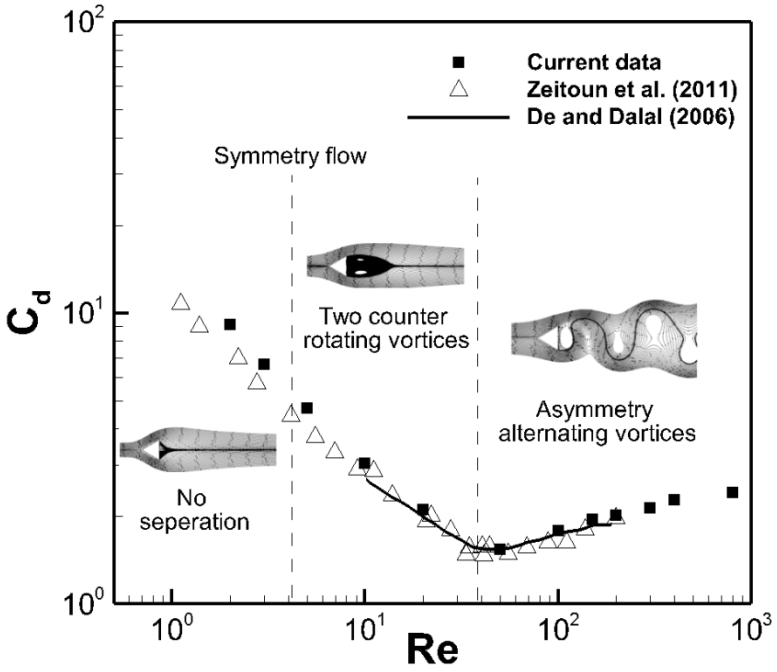


**Fig. 2** Comparison of the drag coefficient.

4.2. Effects of Reynolds and Mach number in pure gas flow

Most previous studies have only considered low Mach numbers within the incompressible limit (M<0.3). However, the present density-based scheme enables high Mach number flows to be considered, from subsonic to supersonic far beyond the incompressible limit. Here we investigate the effects of Reynolds number on low and high Mach number flows, as well as the effects of Mach number on Reynolds number flow below and above the critical Reynolds number. In all the simulations of the current study the cost-effective and carbuncle-free local Lax-Friedrichs (LLF) (or Rusanov [57]) scheme for the inviscid flux and the first method of Bassi and Rebay [28] (also referred to as BR1) are applied.

*4.2.1. Effects of Reynolds number on low Mach number incompressible flows*

The effects of Reynolds number on low Mach number incompressible flows have been extensively investigated in the past. We study these flow cases mainly for the purpose of verifying the present density-based scheme in low Mach number flows. As can be seen in **Fig. 3**, the patterns of streamlines are in excellent accordance with the well-known physics in this type of flows, i.e., the transition from no separation state to two symmetrical vortices followed by two alternating vortexes with increasing Reynolds number.

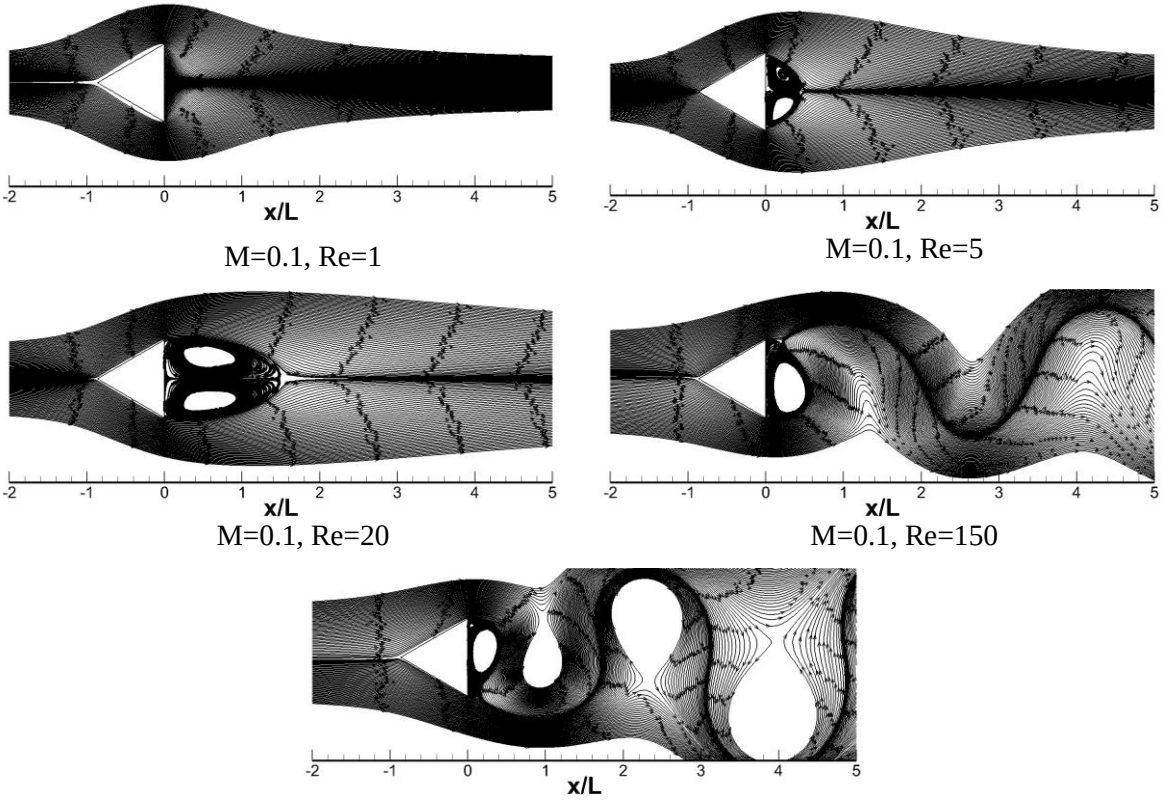


M=0.1, Re=1 M=0.1, Re=5

M=0.1, Re=20 M=0.1, Re=150

M=0.1, Re=800

**Fig. 3** Effects of Reynolds number on low Mach number incompressible flow.

*4.2.2. Effects of Reynolds number on high Mach number supersonic compressible flows*

We also studied the effects of Reynolds number on supersonic compressible flows. The $Re_{cr}$ (which marks the transition from steady to unsteady flow structure) is much higher when compressibility effects are present. As evident from **Fig. 4**, the increase in Mach number substantially hinders the separation and transition processes. The $Re_{cr}$ in the incompressible flow is known to be around 40. In the present compressible flows, no unsteady behavior is observed in flows well above the critical Reynolds number, as high as Re=200. Moreover, it can be seen that the topology of the bubble geometry (semi-triangular shape) is very different compared to the case when the Mach number is small (semi-elliptical shape).

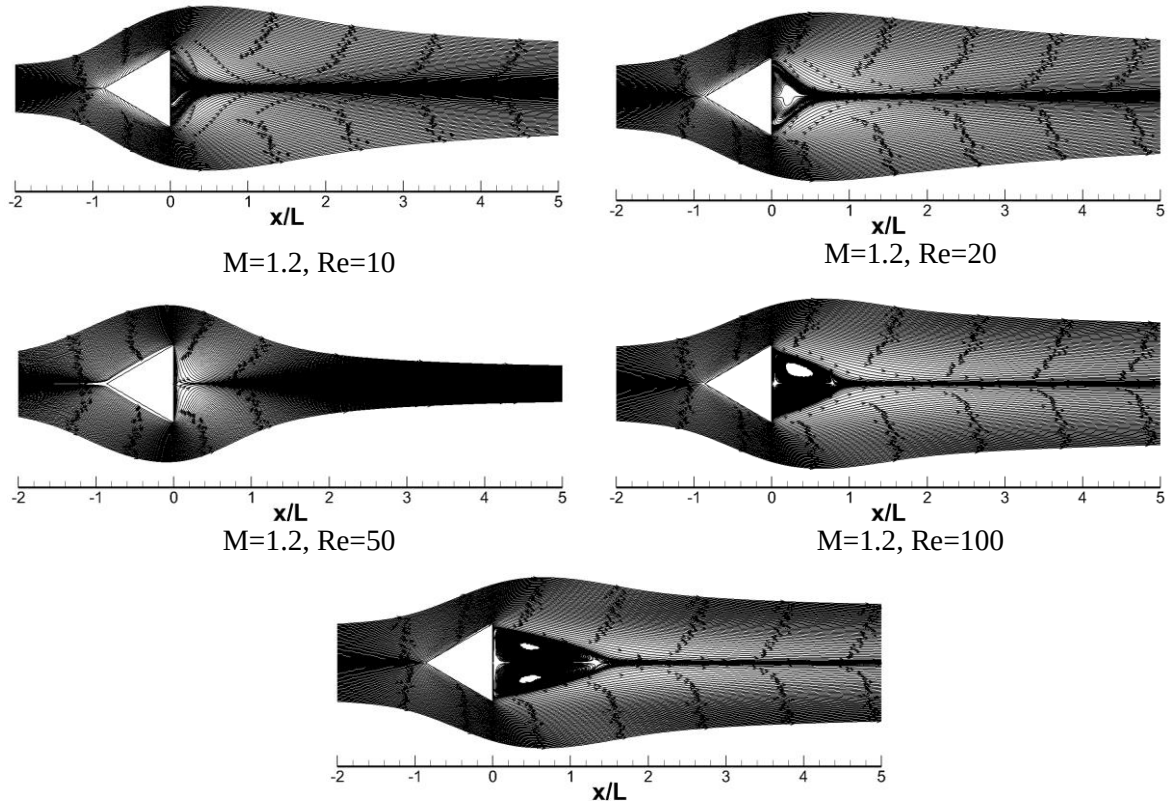


M=1.2, Re=10 M=1.2, Re=20

M=1.2, Re=50 M=1.2, Re=100

M=1.2, Re=200

**Fig. 4** Effects of Reynolds number on high Mach number supersonic compressible flow.

*4.2.3. Effects of Mach number on Reynolds number flows below $Re_{cr}$*

The effects of Mach number on Reynolds number flows below $Re_{cr}$ are shown in **Fig. 5**. It can be observed that with increasing Mach number, the symmetrical vortices shrink in size. For M=2, there is no separation, and thus no vortices are observed.

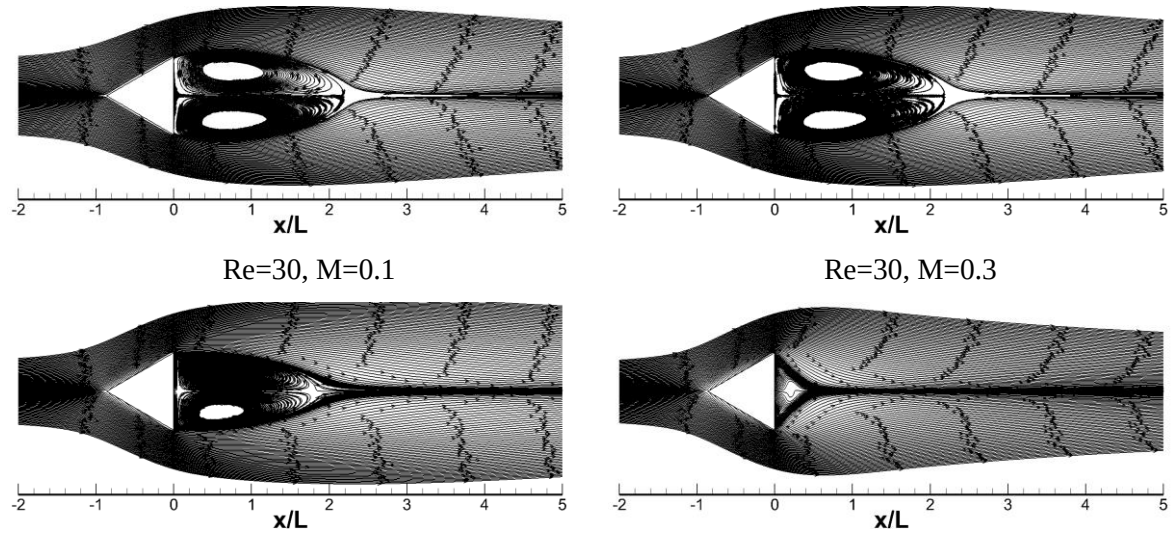


Re=30, M=0.1 Re=30, M=0.3

Re=30, M=0.8 Re=30, M=1.2

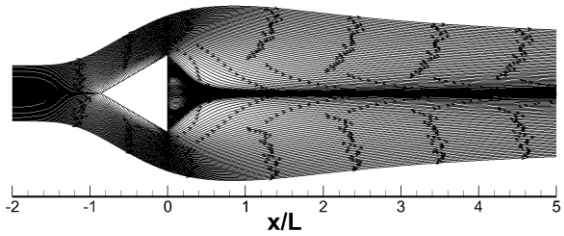


Re=30, M=2.0

**Fig. 5** Effects of Mach number on the flow with Re below the critical Reynolds number.

*4.2.4. Effects of Mach number on Reynolds number flows above $Re_{cr}$*

We investigate the effects of Mach number on Reynolds number flows above $Re_{cr}$. As can be seen in **Fig. 6**, an increase in Mach number results in a decrease in amplitude and an increase in the frequency of oscillations in the drag coefficients. For the high transonic flow (M=1.2), this oscillatory behavior has almost vanished. Virtually no oscillations are observed in the case of the supersonic flow (M=2.0). The snapshots of instantaneous vorticity and streamlines are plotted for two subsonic cases in **Fig. 7** and for two supersonic cases in **Fig. 8**.

**Fig. 7** illustrates the transient behavior of vortices and how this transient behavior changes depending on the Mach number. As indicated in **Fig. 6**, oscillations in the drag coefficient are reduced with increasing Mach number, and increasing the Mach number will stabilize the flow. For Mach numbers corresponding to supersonic regimes, the von Kármán vortex street changes into two symmetrical counter-rotating vortices as shown in **Fig. 8**. The topologies of these vortices are, however, very different from the symmetrical vortices that appear in the low Reynolds and low Mach number regimes.

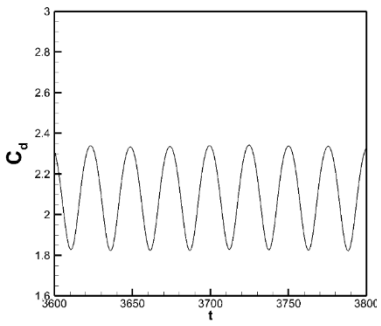


Re=250, M=0.1

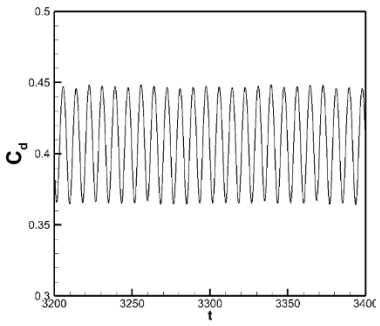


Re=250, M=0.3

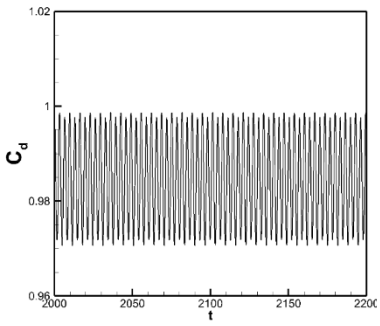


Re=250, M=0.8

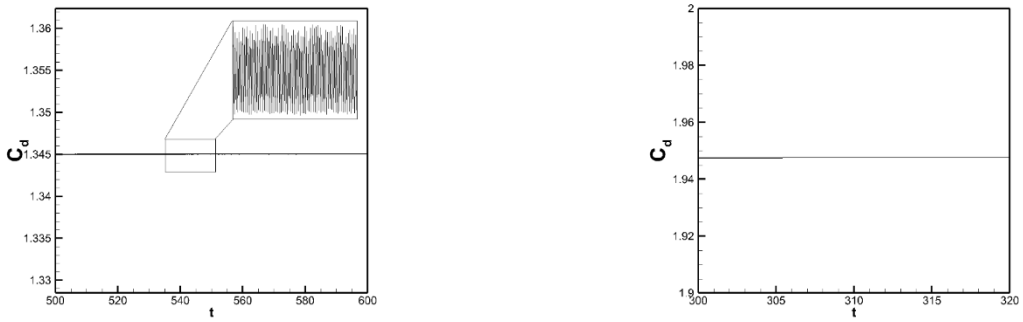


Re=250, M=1.2 Re=250, M=2.0

**Fig. 6** Effects of Mach number on drag coefficient in flow with Re above the critical Reynolds number.

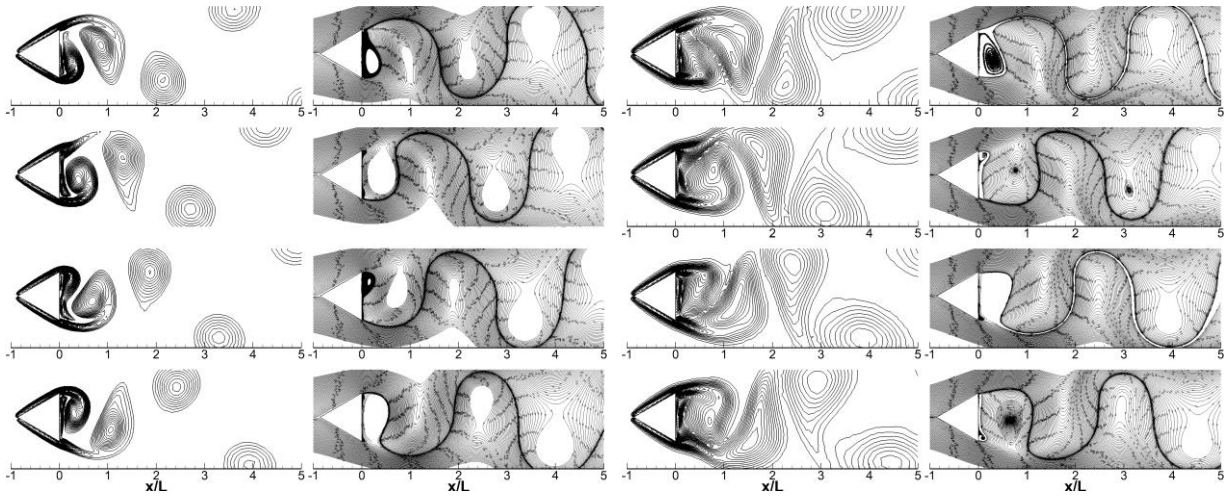


(a) Re=250, and M=0.1 (b) Re=250, and M=0.8

**Fig. 7** Snapshots of instantaneous vorticity (left) and streamlines (right) in different time steps within a shedding cycle for subsonic Mach numbers (a) 0.1 and (b) 0.8.

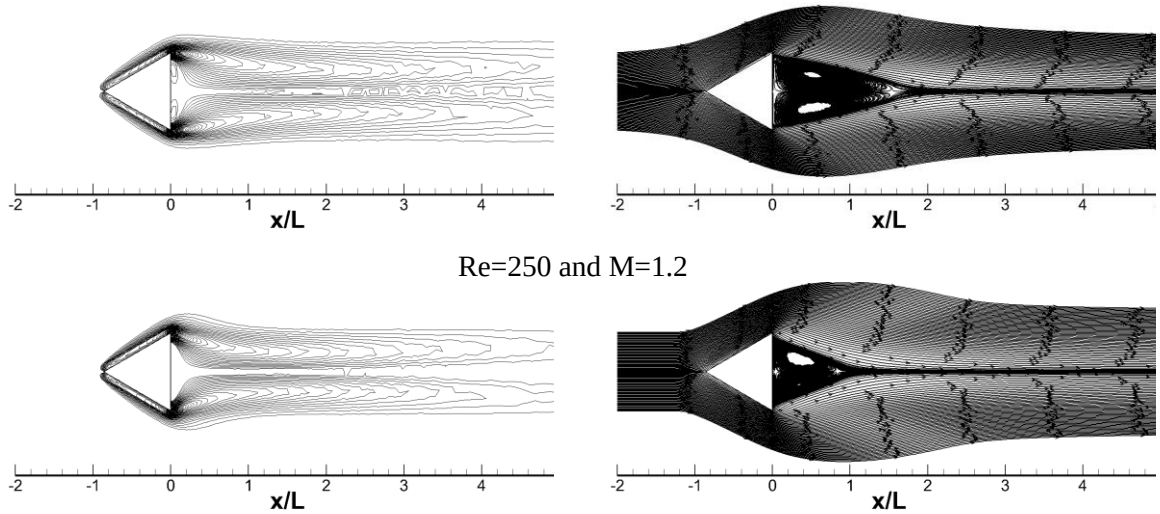


Re=250 and M=1.2

Re=250 and M=2.0

**Fig. 8** Snapshots of instantaneous vorticity (left) and streamlines (right) for supersonic Mach numbers 1.2 and 2.0.

4.3. Effects of Reynolds and Mach number in multiphase flows

We now investigate the effects of added particles on the stability of the flow, the streamline patterns, and coherent structures like vorticities. The properties of the particles were set to be equivalent to those of glass beads with a particle density of 2,500 kg/m$^3$ and a specific heat of 718 J/kg·K. In all the simulation test cases, the particle diameter is assumed to be equal to 20 μm.

*4.3.1. Effects of adding particles within the incompressible limit*

We first investigate the effects of the addition of particles with different particulate loadings on a low Reynolds and low Mach number flow with Re=30 and M=0.1. In the case of pure gas, as shown in **Fig. 5**, two counter-rotating vortices are formed on the backside of the prism. On the other hand, the particulate loading tends to destabilize the flow, as demonstrated in **Fig. 9**. While the addition of particles has no visible effect on the behavior of the flow and the shape of the symmetrical vortices in low particulate loading cases ($\beta$<0.1), in higher particulate loading cases ($\beta$>0.5), unsteady behavior and the formation of von Kármán vortex street are observed.

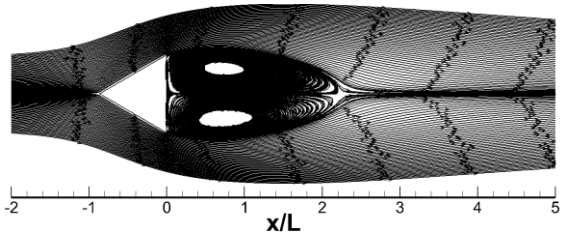


Re=30, M=0.1, $\beta$=0.0

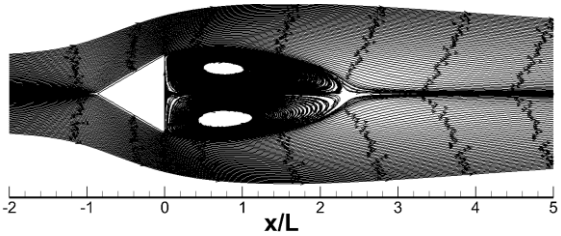


Re=30, M=0.1, $\beta$=0.05

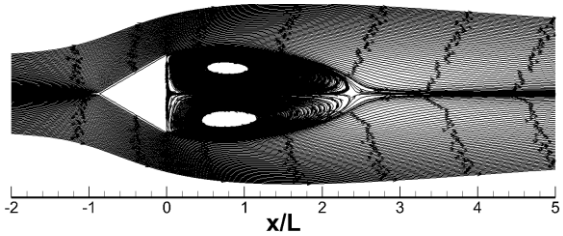


Re=30, M=0.1, $\beta$=0.1

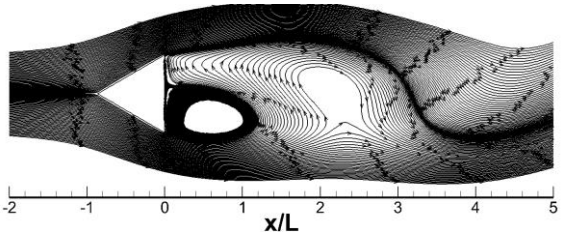


Re=30, M=0.1, β=0.5

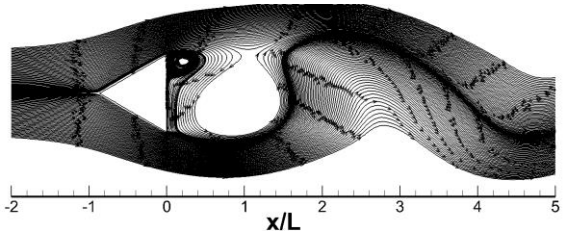


Re=30, M=0.1, $\beta$=1.0

**Fig. 9** Effects of particulate loading ($\beta$) on the low Reynolds and low Mach number flows.

We also investigated the effects of particulate loading in the flow above the critical Reynolds number (Re=250) within the incompressible limit (M=0.1). The unsteady behaviors of drag coefficients ($C_d$) are plotted in **Fig. 10** for increasing particulate loadings. Interestingly, the drag coefficients show a regular periodic behavior until $\beta$=0.5, and they begin to show irregular chaotic behavior in high particle loading cases. The higher the particulate loading, the higher the degree of disorder becomes in the flow patterns.

When the drag coefficients of the high particle loading cases were analyzed more carefully, their behaviors consisted of two components: one regular periodic motion with a time scale of 25 units, and another irregular chaotic motion with a much smaller time scale, as clearly shown for cases $\beta$=0.5 and 1.0 in **Fig. 10**. The second component, which is absent in the case of pure gas as shown in **Fig. 10**, is a new phenomenon, and its origin is directly related to two-way coupling effects between the gas phase and solid phase in multiphase flows. Details of this irregular chaotic behavior can be explained using snapshots of the vorticities and streamlines in **Fig. 11**. Specifically, the vorticity snapshots show how the irregular chaotic behaviors are generated near the solid walls as the vortices are shed from the prism.

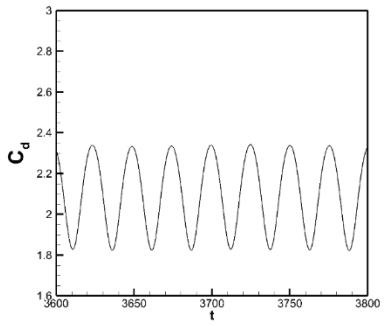


$\beta$=0.0

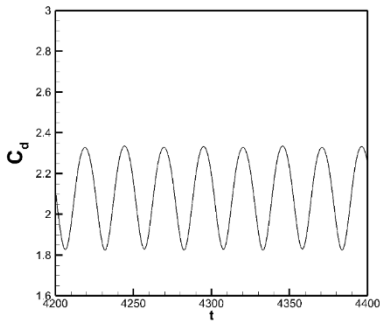


$\beta$=0.01

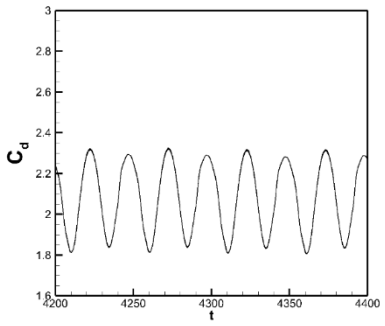


$\beta$=0.05

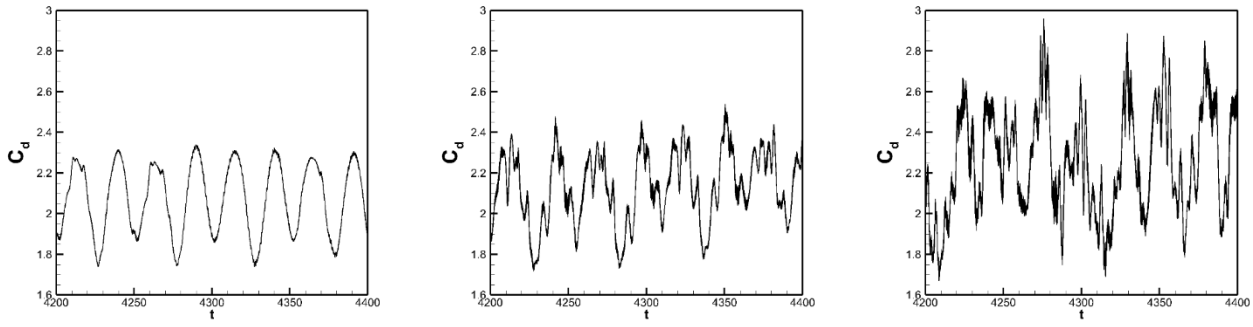


$\beta$=0.1 $\beta$=0.5 $\beta$=1.0

**Fig. 10** Effects of particulate loading on drag coefficients in the flow (Re=250, M=0.1) above the critical Reynolds number and within the incompressible limit.

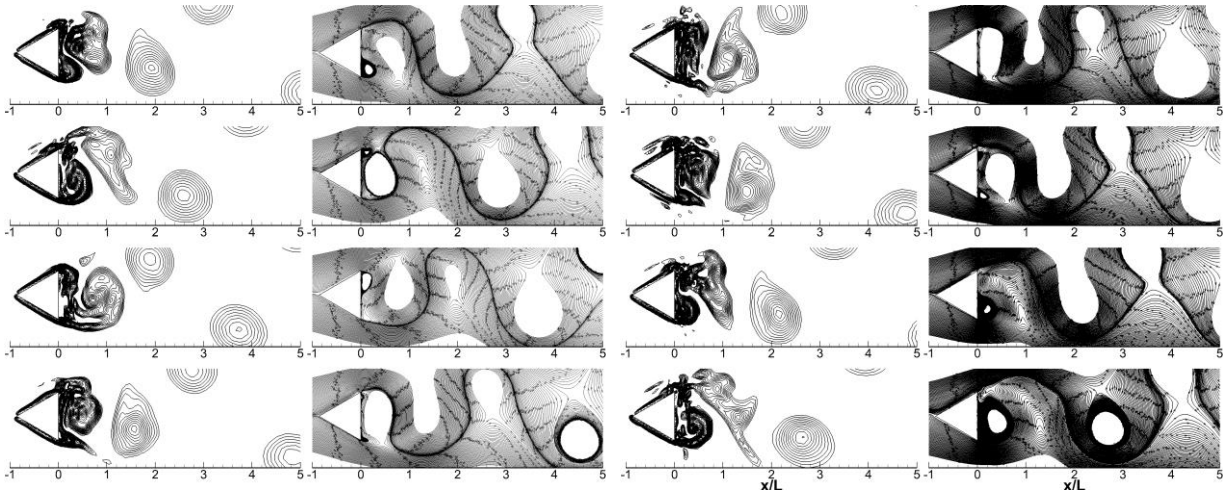


(a) Re=250, and M=0.1, $\beta$=0.5 (b) Re=250, and M=0.1, $\beta$=1.0

**Fig. 11** Snapshots of instantaneous vorticity (left) and streamlines (right) in different time steps within a shedding cycle for different particulate loadings (a) $\beta$=0.5 and (b) $\beta$=1.0.

*4.3.2. Effect of adding particles beyond the incompressible limit*

We further investigated the effects of adding particles with different particulate loadings on flow patterns in the flows below and above the critical Reynolds number (Re=30 and 250) beyond the incompressible limit (M=1.2). In the flow below the critical Reynolds number (Re=30), adding particles to the gas flow led to an increase in the size of the symmetrical vortices, as shown in **Fig. 12**.

On the other hand, in the flow above the critical Reynolds number (Re=250), adding particles produced flow instability when the particulate loading was above a threshold value, as shown in **Fig. 13**. This is in stark contrast with the pure gas case (Re=200, M=1.2, β=0.0) shown in **Fig. 13** where no flow instability was observed due to the compressibility effect.

However, in the cases of multiphase flows (Re=250, M=1.2, β=0.5, 1.0) in **Fig. 13**, the two-way coupling effects between the gas phase and solid phase override the compressibility effect, causing severe flow instability and spontaneous symmetry breaking of the coherent dynamics of the vortices.

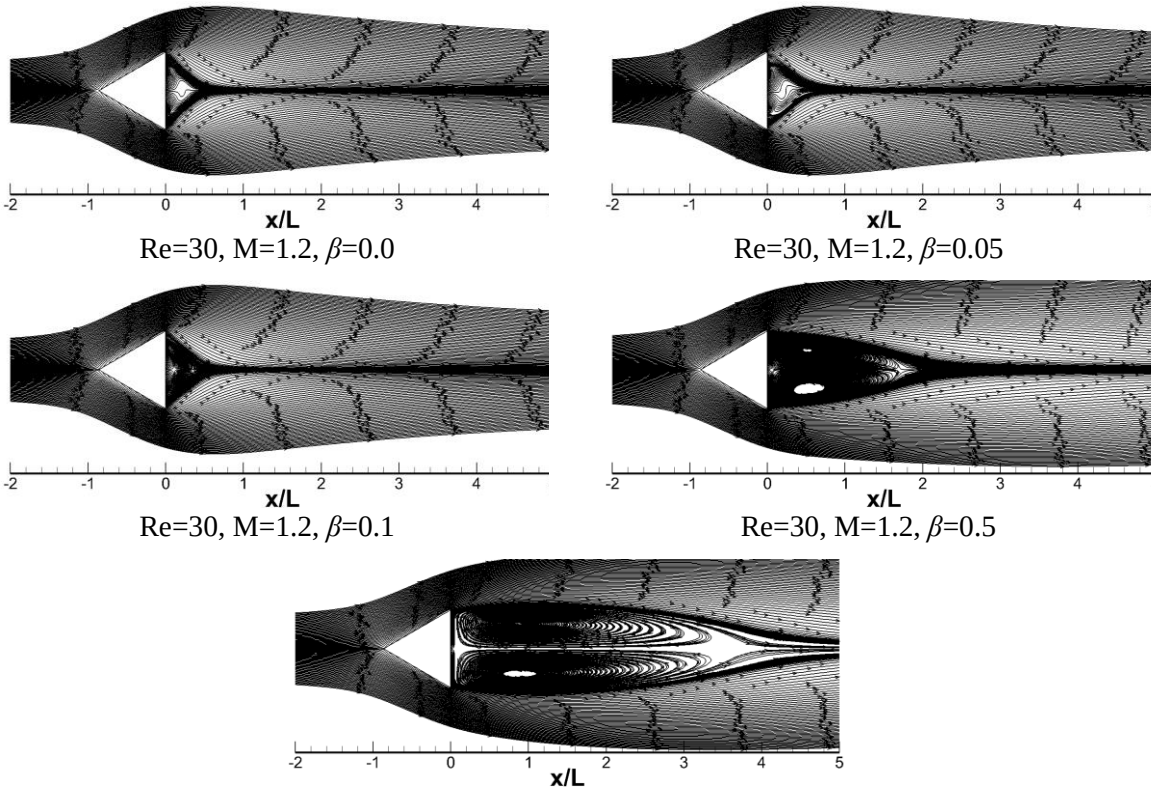


Re=30, M=1.2, $\beta$=0.0 Re=30, M=1.2, $\beta$=0.05

Re=30, M=1.2, $\beta$=0.1 Re=30, M=1.2, $\beta$=0.5

Re=30, M=1.2, $\beta$=1.0

**Fig. 12** Effects of particulate loading ($\beta$) on flow patterns in the flow (Re=30, M=1.2) below the critical Reynolds number and beyond the incompressible limit.

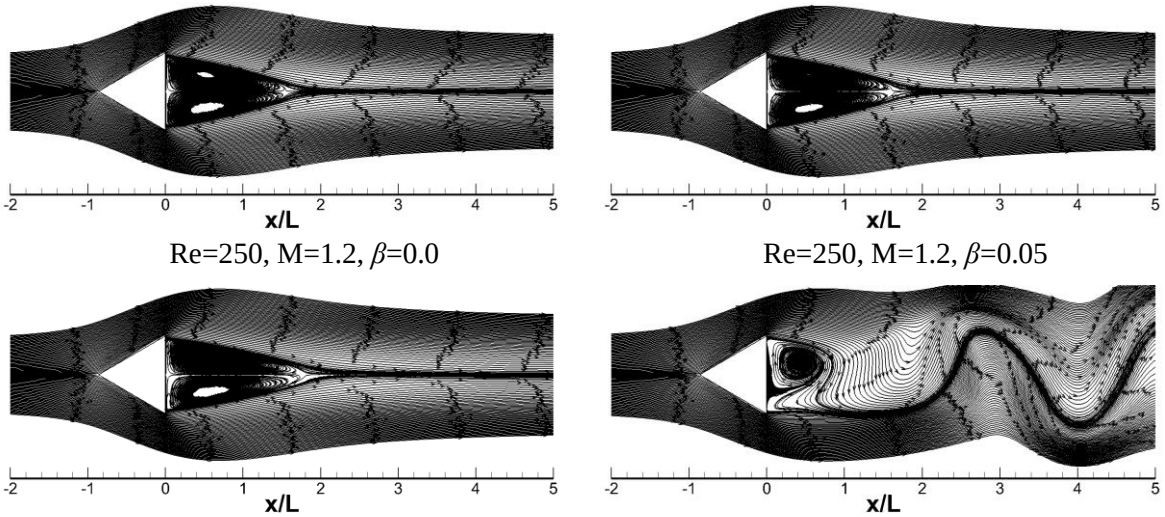


Re=250, M=1.2, $\beta$=0.0 Re=250, M=1.2, $\beta$=0.05

Re=250, M=1.2, $\beta$=0.1 Re=250, M=1.2, $\beta$=0.5

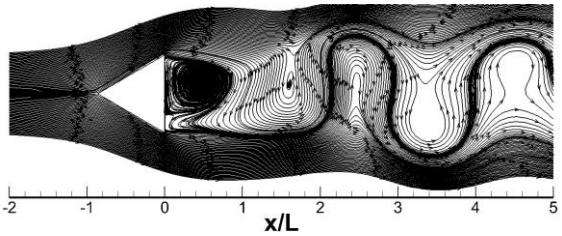


Re=250, M=1.2, $\beta$=1.0

**Fig. 13** Effects of particulate loading ($\beta$) on flow patterns in the flow (Re=250, M=1.2) above the critical Reynolds number and beyond the incompressible limit.

*4.3.3. On the role of the Stokes number on the behavior of the bubbles and shedding*

As mentioned by Green [58], both the particle parameters and the carrier phase properties play a significant role in the dispersion of the particles by the vortices. The level of interaction between the gas and particles depends on the Stokes number which characterizes the relaxation time of the particles in comparison with the time scale of the fluid flow:

$$St = \frac{\tau_V}{t_{ref}}. \tag{32}$$

In this relation, $t_{ref}$ is a reference time which can be defined as the characteristic length divided by the characteristic speed, and $\tau_V$ is the momentum (velocity) response time of the particles given by

$$\tau_V = \frac{\rho_s d^2}{18\mu_g}. \tag{33}$$

As schematically shown in **Fig. 14**, for very small particles ($St \ll 1$), the particulate phase is in dynamic equilibrium with the carrier gas phase. Therefore particles will closely follow the streamlines of the vortical flow. On the other hand, large particles ($St \gg 1$) will not be affected by the vortices of the fluid flow because of their large inertia. Therefore, there may be an intermediate case where intermediate particle sizes ($St \approx 1$) tend to be centrifuged from the vortex cores and accumulate at the edge of the vortices, leading to inhomogeneous particle concentrations.

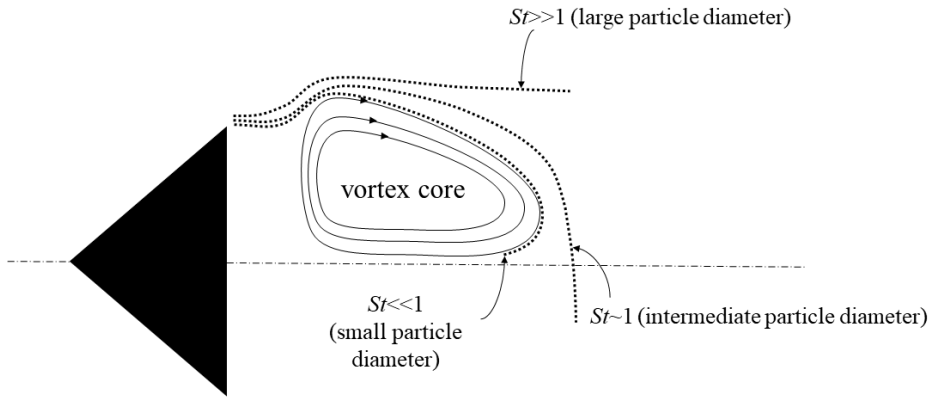


**Fig. 14** The schematic representation of the effect of the Stokes number on particle dispersion in vortices.

A similar explanation can be applied to the effects of the variation in Stokes number depending on the fluid condition. In **Fig. 15**, the velocity vectors of the dust phase and gas phase are compared for two different Mach and Reynolds numbers. In both cases, as the flow is decelerated behind the prism, particles cannot follow the gas phase trajectory. When the Reynolds number is low (Re=30), particles can follow the streamlines of the carrier gas. In this subcritical Reynolds number flow, with increasing Mach number, the velocity vectors of the particles show only a slight deviation from those in the gas.

However, when the Reynolds number is large enough (Re=250), and belongs to the supercritical Reynolds number flow, deviation of the particle path from the gas becomes significant. Unlike the case with the subcritical Reynolds number flow, with low Mach number flow, this deviation is more critical, resulting in irregular chaotic behavior in the flow patterns. As explained in subsection 4.3.1 and illustrated further in the case of Re=250, M=0.1, $\beta$=1.0 in **Fig. 15**, it is the two-way coupling mechanisms between the carrier gas phase and the solid particle phase that drastically change the flow patterns in the gas phase, which is initially in the range of laminar flow.

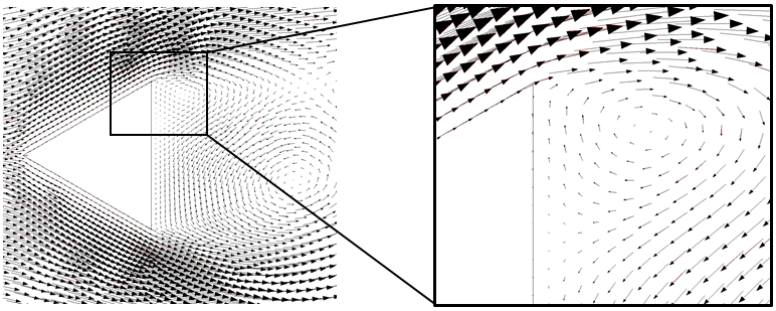

Re=30, M=0.1, $\beta$=1.0

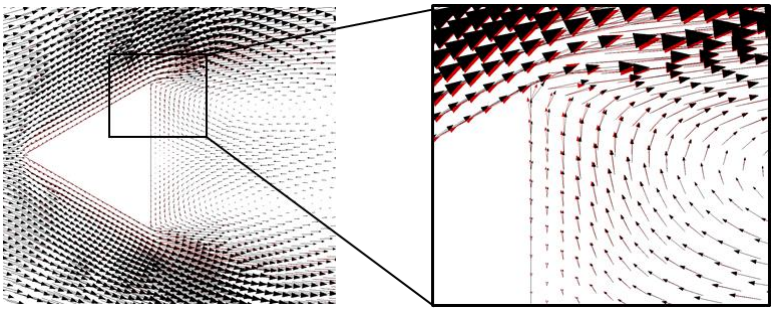

Re=30, M=1.2, $\beta$=1.0

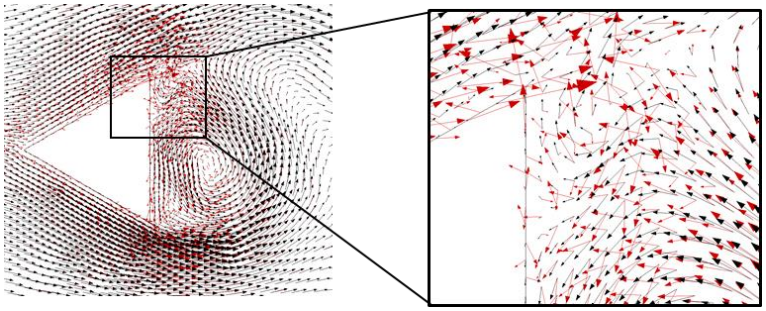

Re=250, M=0.1, $\beta$=1.0

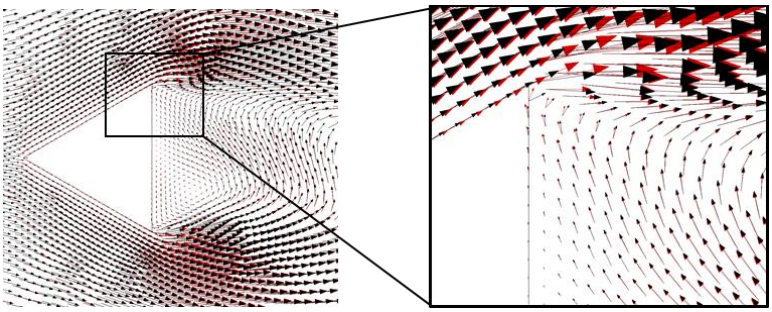

Re=250, M=1.2, $\beta$=1.0

**Fig. 15** Effects of fluid properties on particle dispersion in vortices using velocity vectors of gas (black) and solid (red) phases.

## 5. Concluding remarks

The problem of external flows past bluff bodies has remained one of the fundamental subjects in fluid dynamics. Great efforts have been devoted to not only understand general flow patterns like the formation of the wake and the onset of vortex shedding in the flow but

also to investigate crucial flow features like time-averaged drag coefficients and forced convection heat transfer.

In this work, we simulated dusty gas flows past a prism with a focus on the role of Reynolds and Mach numbers on laminar multiphase flow. A density-based solver in the Eulerian-Eulerian framework was developed using a modal discontinuous Galerkin method. This solver allowed compressibility effects to be considered, and, as a result, enabled the investigation of a much wider range of Mach numbers, from subsonic to supersonic regimes.

In particular, the effects of added dust particles on the flow patterns and crucial flow features were investigated in a two-fluid model framework. A simple strategy (borrowed from computational magnetohydrodynamics and atmospheric icing) to circumvent the numerical difficulty resulting from the non-strictly hyperbolic nature of the model equation of the solid phase was also introduced. Then, for various combinations of flow parameters, the effects of the addition of dust particles with different particulate loadings were investigated, and several new physical phenomena were observed.

For example, it was shown that an increase in the Mach number stabilizes the flow, i.e., hinders the transition from stationary to unsteady. Also, it was found that, in a low Mach number flow, the addition of dust particles having the properties of glass beads and a diameter of 20 μm can destabilize the flow, which is in accordance with previous findings. On the other hand, in stark contrast with the pure gas case above the critical Reynolds number in the supersonic regime, where no flow instability was observed, adding particles produced flow instability in the multiphase flows. Finally, a discussion on the role of the Stokes number on the behavior of the bubbles and shedding was presented.

Several issues remain that deserve further attention. First, more detailed parametric studies on the solid phase parameters including the particle diameter and mass will be needed. Also, it will be interesting to explore the problem of defining the critical Reynolds number for the onset of vortex shedding in different Mach regimes, and also for different particulate loadings, by following the studies of Goujon-Durand *et al*. [14] and Dušek *et al*. [59]. This will require conducting comprehensive simulations and recording the $x$ and $y$-direction velocities in a set of history points along the axis (global mode analysis).

Moreover, investigation of the rarefaction effects in terms of Knudsen number in conjunction with the presence of particles, using a second-order constitutive relationship [60-

62] for the gas phase beyond the present first-order Navier-Stokes-Fourier relationship, will be an important topic. We hope to report the investigation of these subjects in the future.

**Acknowledgments**

This work was supported by the National Research Foundation of Korea (NRF 2017-R1A5A1015311), South Korea. The first author (O.E.) acknowledges the support provided by the Korea Institute of Science and Technology Information (KISTI), South Korea.

**References**

[1] Davis RW, Moore E. A numerical study of vortex shedding from rectangles. Journal of Fluid Mechanics. 1982;116:475-506.
[2] Okajima A. Strouhal numbers of rectangular cylinders. Journal of Fluid Mechanics. 1982;123:379-398.
[3] Tamura T, Kuwahara K. Numerical study of aerodynamic behavior of a square cylinder. Journal of Wind Engineering and Industrial Aerodynamics. 1990;33:161-170.
[4] Kelkar KM, Patankar SV. Numerical prediction of vortex shedding behind a square cylinder. International Journal for Numerical Methods in Fluids. 1992;14:327-341.
[5] Williamson CH. Vortex dynamics in the cylinder wake. Annual Review of Fluid Mechanics. 1996;28:477-539.
[6] Zdravkovich MM. Flow around Circular Cylinders: Volume 2: Applications: Oxford university press; 1997.
[7] Lee T. Early stages of an impulsively started unsteady flow past non-rectangular prisms. Computers & Fluids. 1998;27:435-453.
[8] Saha A, Biswas G, Muralidhar K. Three-dimensional study of flow past a square cylinder at low Reynolds numbers. International Journal of Heat and Fluid Flow. 2003;24:54-66.
[9] Sharma A, Eswaran V. Heat and fluid flow across a square cylinder in the two-dimensional laminar flow regime. Numerical Heat Transfer, Part A: Applications. 2004;45:247-269.
[10] Ahn HT. Hyperbolic cell-centered finite volume method for steady incompressible Navier-Stokes equations on unstructured grids. Computers & Fluids. 2020:104434.
[11] Cao Y, Tamura T, Kawai H. Spanwise resolution requirements for the simulation of high-Reynolds-number flows past a square cylinder. Computers & Fluids. 2020;196:104320.
[12] Jackson C. A finite-element study of the onset of vortex shedding in flow past variously shaped bodies. Journal of Fluid Mechanics. 1987;182:23-45.
[13] Zielinska B, Wesfreid J. On the spatial structure of global modes in wake flow. Physics of Fluids. 1995;7:1418-1424.
[14] Goujon-Durand S, Jenffer P, Wesfreid J. Downstream evolution of the Bénard–von Kármán instability. Physical Review E. 1994;50:308.
[15] Wesfreid J, Goujon-Durand S, Zielinska B. Global mode behavior of the streamwise velocity in wakes. Journal de Physique II. 1996;6:1343-1357.
[16] Johansson SH, Davidson L, Olsson E. Numerical simulation of vortex shedding past triangular cylinders at high Reynolds number using a k-ε turbulence model. International Journal for Numerical Methods in Fluids. 1993;16:859-878.
[17] De AK, Dalal A. Numerical simulation of unconfined flow past a triangular cylinder. International Journal for Numerical Methods in Fluids. 2006;52:801-821.
[18] Prhashanna A, Sahu AK, Chhabra R. Flow of power-law fluids past an equilateral triangular cylinder: Momentum and heat transfer characteristics. International Journal of Thermal Sciences. 2011;50:2027-2041.
[19] Chatterjee D, Mondal B. Forced convection heat transfer from an equilateral triangular cylinder at low Reynolds numbers. Heat and Mass Transfer. 2012;48:1575-1587.

[20] Rahimi A, Ejtehadi O, Lee KH, Myong RS. Near-field plume-surface interaction and regolith erosion and dispersal during the lunar landing. Acta Astronautica. 2020;175:308-326.
[21] Crowe CT, Troutt TR, Chung JN. Particle Interactions with Vortices. In: Green SI, editor. Fluid Vortices. Dordrecht: Springer Netherlands; 1995. p. 829-861.
[22] Hunt J. Industrial and environmental fluid mechanics. Annual Review of Fluid Mechanics. 1991;23:1-42.
[23] Saffman P. On the stability of laminar flow of a dusty gas. Journal of Fluid Mechanics. 1962;13:120-128.
[24] Damseh RA. On boundary layer flow of a dusty gas from a horizontal circular cylinder. Brazilian Journal of Chemical Engineering. 2010;27:653-662.
[25] Mehrizi AA, Farhadi M, Shayamehr S. Natural convection flow of Cu–Water nanofluid in horizontal cylindrical annuli with inner triangular cylinder using lattice Boltzmann method. International Communications in Heat and Mass Transfer. 2013;44:147-156.
[26] Xu J, Zhang J, Wang H, Mi J. Fine Particle Behavior in the Air Flow Past a Triangular Cylinder. Aerosol Science and Technology. 2013;47:875-884.
[27] Bai B, Li X. Deposition of particles in the supersonic flow past a wedge. Powder Technology. 2016;304:268-273.
[28] Bassi F, Rebay S. A high-order accurate discontinuous finite element method for the numerical solution of the compressible Navier–Stokes equations. Journal of Computational Physics. 1997;131:267-279.
[29] Cockburn B, Shu CW. The Runge–Kutta discontinuous Galerkin method for conservation laws V: multidimensional systems. Journal of Computational Physics. 1998;141:199-224.
[30] Zhang X, Shu CW. On positivity-preserving high order discontinuous Galerkin schemes for compressible Euler equations on rectangular meshes. Journal of Computational Physics. 2010;229:8918-8934.
[31] Zhang X, Xia Y, Shu CW. Maximum-principle-satisfying and positivity-preserving high order discontinuous Galerkin schemes for conservation laws on triangular meshes. Journal of Scientific Computing. 2012;50:29-62.
[32] Franquet E, Perrier V. Runge–Kutta discontinuous Galerkin method for reactive multiphase flows. Computers & Fluids. 2013;83:157-163.
[33] Kontzialis K, Ekaterinaris JA. High order discontinuous Galerkin discretizations with a new limiting approach and positivity preservation for strong moving shocks. Computers & Fluids. 2013;71:98-112.
[34] Xiao H, Myong R. Computational simulations of microscale shock–vortex interaction using a mixed discontinuous Galerkin method. Computers & Fluids. 2014;105:179-193.
[35] Lu H, Zhu J, Wang D, Zhao N. Runge–Kutta discontinuous Galerkin method with front tracking method for solving the compressible two-medium flow. Computers & Fluids. 2016;126:1-11.
[36] Coulette D, Franck E, Helluy P, Mehrenberger M, Navoret L. High-order implicit palindromic discontinuous Galerkin method for kinetic-relaxation approximation. Computers & Fluids. 2019;190: 485-502.
[37] Landet T, Mardal K-A, Mortensen M. Slope limiting the velocity field in a discontinuous Galerkin divergence-free two-phase flow solver. Computers & Fluids. 2020;196:104322.
[38] Ishii R, Umeda Y, Yuhi M. Numerical analysis of gas-particle two-phase flows. Journal of Fluid Mechanics. 1989;203:475-515.
[39] Kim SW, Chang KS. Reflection of shock wave from a compression corner in a particle-laden gas region. Shock Waves. 1991;1:65-73.
[40] Saito T. Numerical analysis of dusty-gas flows. Journal of Computational Physics. 2002;176:129-144.
[41] Igra O, Hu G, Falcovitz J, Wang B. Shock wave reflection from a wedge in a dusty gas. International Journal of Multiphase Flow. 2004;30:1139-1169.
[42] Miura H, Glass II. On a dusty-gas shock tube. Proceedings of the Royal Society of London A: Mathematical, Physical and Engineering Sciences. 1982;382:373-388.
[43] Dobran F, Neri A, Macedonio G. Numerical simulation of collapsing volcanic columns. Journal of Geophysical Research: Solid Earth. 1993;98:4231-4259.

[44] Ejtehadi O, Rahimi A, Karchani A, Myong R. Complex wave patterns in dilute gas–particle flows based on a novel discontinuous Galerkin scheme. International Journal of Multiphase Flow. 2018;104:125-151.
[45] Zhang X, Shu CW. Positivity-preserving high order discontinuous Galerkin schemes for compressible Euler equations with source terms. Journal of Computational Physics. 2011;230:1238-1248.
[46] Zhang X, Shu CW. On maximum-principle-satisfying high order schemes for scalar conservation laws. Journal of Computational Physics. 2010;229:3091-3120.
[47] Barth TJ, Jespersen DC. The design and application of upwind schemes on unstructured meshes. 27th Aerospace Sciences Meeting: AIAA Paper 1989-0368; 1989.
[48] Powell KG, Roe PL, Myong RS, Gombosi T. An upwind scheme for magnetohydrodynamics. 12th Computational Fluid Dynamics Conference: AIAA Paper 1995-1704; 1995.
[49] Powell KG, Roe PL, Linde TJ, Gombosi TI, De Zeeuw DL. A solution-adaptive upwind scheme for ideal magnetohydrodynamics. Journal of Computational Physics. 1999;154:284-309.
[50] Janhunen P. A positive conservative method for magnetohydrodynamics based on HLL and Roe methods. Journal of Computational Physics. 2000;160:649-61.
[51] Jung S, Myong RS. A second-order positivity-preserving finite volume upwind scheme for air-mixed droplet flow in atmospheric icing. Computers & Fluids. 2013;86:459-69.
[52] van der Hoef MA, Ye M, van Sint Annaland M, Andrews AT, Sundaresan S, Kuipers JAM. Multiscale Modeling of Gas-Fluidized Beds. Advances in Chemical Engineering. 2006;31:65-149.
[53] Zeitoun O, Ali M, Nuhait A. Convective heat transfer around a triangular cylinder in an air cross flow. International Journal of Thermal Sciences. 2011;50:1685-1697.
[54] Ejtehadi O, Rahimi A, Myong RS. Numerical investigation of the counter-intuitive behavior of Mach disk movement in underexpanded gas-particle jets. Journal of Computational Fluid Engineering. 2019;24:19-28.
[55] Ejtehadi O, Myong RS. A modal discontinuous Galerkin method for simulating dusty and granular gas flows in thermal non-equilibrium in the Eulerian framework. Journal of Computational Physics. 2020;411:109410.
[56] Ejtehadi O, Rahimi A, Myong RS. Investigation of a trifold interaction mechanism of shock, vortex, and dust using a DG method in a two-fluid model framework. Powder Technology. 2020;374:121-138.
[57] Rusanov VV. Calculation of interaction of non-steady shock waves with obstacles: NRC, Division of Mechanical Engineering; 1962.
[58] Green S. Fluid vortices: Springer Science & Business Media; 2012.
[59] Dušek J, Le Gal P, Fraunié P. A numerical and theoretical study of the first Hopf bifurcation in a cylinder wake. Journal of Fluid Mechanics. 1994;264:59-80.
[60] Myong RS. A computational method for Eu's generalized hydrodynamic equations of rarefied and microscale gasdynamics. Journal of Computational Physics. 2001;168:47-72.
[61] Myong RS. A generalized hydrodynamic computational model for rarefied and microscale diatomic gas flows. Journal of Computational Physics. 2004;195:655-676.
[62] Myong RS. Numerical Simulation of Hypersonic Rarefied Flows Using the Second-Order Constitutive Model of the Boltzmann Equation. Advances in Some Hypersonic Vehicles Technologies: InTech; 2018. http://dx.doi.org/10.5772/intechopen.70657